ELSEVIER

Journal of Nuclear Materials 256 (1998) 235–246

journal of nuclear materials

Recoil tritium in 304-stainless steel: the initial distribution revisited

Abdul R. Dulloo [a,*], Ward S. Diethorn [b]

[a] *Science and Technology Center, Westinghouse Electric Company, Pittsburgh, PA 15235, USA*
[b] *Nuclear Engineering Department, The Pennsylvania State University, University Park, PA 16802, USA*

Received 19 September 1996; accepted 4 March 1998

Abstract

A new experimental determination of the initial (as-deposited) concentration profile of recoil tritons (tritium) in a thick 304-S.S. target is compared with the linear recoil profile predicted by Di Cola/Matzke (DM) theory. Satisfactory agreement is observed. In the experiment, 2.72-MeV tritons produced by the ^{6}Li(n, α)^{3}H reaction in a thick Li_2CO_3 powder inject a thick 304-S.S. slab with tritium. A subsequent acid etch of the slab followed by tritium and stainless steel radioassays yield the concentration profile. Monte Carlo simulations with the SRIM code show that a non-linear profile is expected, with an increasing departure from linearity occurring as the initial triton energy decreases below 2.72 MeV. DM theory is extended to cover in a slab configuration (a) recoil concentration in both source and target with arbitrary thicknesses, and (b) probability density functions describing recoil pathlength and energy distributions in a thick source and target.

1. Introduction

Injection of recoil tritium into materials such as stainless steel, e.g., 2.72-MeV tritons from the thermal neutron-induced ^{6}Li(n, α)^{3}H reaction, provides samples for thermal annealing studies, whose purpose is the evaluation of tritium migration and loss. Studies of this kind address a number of problems in fusion technology. A common practice is to adopt as the initial (as-deposited) distribution of tritium a theoretical, recoil concentration profile derived by Di Cola and Matzke [1,2], but also attributed by others [3–6] to the unpublished work of Beck, their contemporary. There is an extensive literature on tritium recoils in metals [7–15], as well as work on recoil ^{133}Xe[1,5,16], ^{141}Ce [6] and ^{222}Rn [1,16] in metals and oxides. The Di Cola/Matzke (DM) model deals with two cases: slab and sphere targets in contact with a very thin or very thick, uniform source of monoenergetic recoils. Of the two, the sphere is the more fundamental, since the sphere results collapse to the slab results when the appropriate asymptotic limit is taken.

In the DM model, monoenergetic source recoils are emitted isotropically at a constant, uniform generation rate. At a given source position, recoils emitted into the same differential solid angle there come to rest after traveling identical, straight-line pathlengths. A key assumption is the form of the linkage equation connecting the recoil pathlengths l_j, $j = s, t$, in source (s) and target (t) with the corresponding ranges R_s and R_t of the as-produced recoils:

$$\frac{l_s}{R_s} + \frac{l_t}{R_t} = 1. \tag{1}$$

Di Cola and Matzke gave 'linear energy loss' as the reason for their adoption of Eq. (1), presumably meaning that a constant recoil stopping power, dE/dl_j, is the underlying rationale. But, this condition is much too restrictive. For example, the proportionality $dE/dl_j \propto 1/E^{\alpha}$ yields Eq. (1) for any value of α, not just $\alpha = 0$.

For a slab target with thickness R_t in one-sided contact with a thick source, the DM model predicts an initial recoil distribution, $C(x_t)$, versus depth x_t, that

* Corresponding author. Fax: +1-412 256 1222; e-mail: dullooar@westinghouse.com.

0022-3115/98/$19.00
PII: S0022-3115(98)00048-8

decreases linearly with increasing x_t. A companion initial distribution, $C(x_s)$, of recoils deposited in the source was not covered by Di Cola and Matzke. Eq. (1) of course is not needed in the derivation of $C(x_s)$; rudiments of a theoretical approach to the derivation of $C(x_s)$ can be found in the older literature [17–20]. The general and most informative case, i.e., arbitrary slab target/source thicknesses, is not available in the literature.

Acid etching of a target (or source) followed by assay of recoil atoms in the etchant provides an experimental recoil concentration profile. One such attempt [7] to confirm, in a thick 304 stainless steel slab, a linear $C(x_t)$ for recoil tritium is not convincing. A linear trend in the data is observed only after discarding half the data points, and ignoring both a weak tail in $C(x_t)$ beyond the triton range and a pronounced dip in $C(x_t)$ near the target/source interface. In another example, $C(x_t)$ of fission recoil ^{141}Ce in an iron alloy slab [6] is in substantial agreement with the DM model, but again $C(x_t)$ trails off at the end of the recoil range. Clearly, a linear ^{141}Ce concentration is suspect here, since as-produced fission recoils are not monoenergetic. For this reason, the use in thermal annealing studies of a linear $C(x_t)$ profile for fission recoils is problematic. Polyenergetic recoils obeying $C(x_t)$ linearity at each energy are expected to produce a composite $C(x_t)$ convex to the source/target interface, which is one explanation for the trailing-off of the concentration observed in the ^{141}Ce study.

We revisit the initial concentration of recoil tritium in 304 stainless steel with the objective of comparing a new experimental determination of $C(x_t)$ with that predicted by DM theory and with results generated with the authoritative SRIM code [21,22].

2. Experimental work

2.1. Procedures

Discs, 15 mm in diameter and 0.508 mm thick, were cut from 304-S.S. commercial sheet stock with composition given in Table 1, vacuum-annealed to a grain size of 15 μm following cold-working, and mechanically polished to a final nominal finish of 0.05 μm. A surface oxide film, perhaps several hundred angstroms thick, is undoubtedly present on a polished disc. Each disc is covered (one side only) with a natural Li_2CO_3 powder, mean particle diameter of 2.7 μm and thickness of 50 times the triton range R_s, sealed in a quartz capsule, and irradiated with thermal neutrons for 2 h at 1 MW in the TRIGA reactor facility at The Pennsylvania State University. The resulting 2.72-MeV triton injection produces a typical volume-average tritium concentration of 20 appb in a one-range-thick surface layer of the disc. During the reactor irradiation the capsule is immersed in liquid nitrogen (77 K).

The tritium content of a disc as a function of disc depth is measured by chemically etching the disc with dilute aqua regia, during which the released tritium is radioassayed by scintillation spectroscopy (HTO) of the etchant and as HT in a gas-flow chamber operated in the current mode within the proportional region. Before P-10, the carrier gas, sweeps HT from the etch vessel to the chamber, it is stripped of moisture and acid vapors by sequential water, ethylene glycol and NaOH pellet traps. Less than 0.5% of the etchant tritium (HTO) is transferred to the traps by the carrier gas. The etch depth removed from a disc is calculated from radioassay of ^{51}Cr activity in etchant samples produced by the ^{50}Cr (n,γ) ^{51}Cr reaction in the disc during triton injection. The etch rate is about 1 μm h^{-1}. An error analysis shows that the etch depth is subject to an uncorrelated uncertainty of several percent. A complete description of the experimental techniques is reported elsewhere [23].

An in-reactor experiment with an instrumented (thermocouple) capsule showed that during triton injection the disc temperature rises to about 60°C in the absence of cooling. As discussed subsequently, cooling a disc to 77 K during injection and before the start of etching is necessary to minimize tritium migration and thus distortion of the disc's initial tritium distribution. Following injection, discs are also stored at liquid nitrogen temperature and exposed to room temperature only during the transfer from this coolant to the etch vessel, a procedure requiring a total of about 2 h.

Numerous factors that can potentially perturb the interpretation of the tritium results and the etch depth determinations were systematically evaluated [23] and found to be insignificant. Among these are foreign tritium produced by the fast neutron-induced ^{6}Li(n,α) ^{3}H reaction or (n, triton) reactions in stainless steel, tritium contamination of a disc by traces of residual Li_2CO_3 powder, disc adsorption of HTO/HT released from Li_2CO_3 during injection, tritium exchange between old HTO in the etchant and protium in the carrier gas, and organically bound tritium (OBT) on the disc surface [24,25]. Experiments also eliminated fast-neutron knockout of surface tritium.

Table 1
Composition of 304-stainless steel

Element	Fe [a]	Cr	Ni	Mn	C	Si	Cu	Mo	N	P	S
Weight (%)	69.56	18.45	9.23	1.60	0.059	0.41	0.34	0.28	0.046	0.029	0.002

[a] By difference.

Distillation of etchant after neutralization with Na_2CO_3 eliminated interference from stainless steel activity during HTO radioassay. Complete distillation of an etchant sample, however, is required to avoid isotope fractionation of tritium, which during a partial distillation depletes the distillate of HTO by up to 6%. Significant tritium leakage (predominantly as HTO) occurs at a rate of several percent per day when a disc is stored at room temperature prior to etching. Disc storage at liquid nitrogen temperature eliminates this source of error. Austin [7] reported that room-temperature leakage of tritium was insignificant, but he apparently searched for HT leakage only.

Three additional perturbing factors in an etch depth determination were examined: etching homogeneity, pitting corrosion, and disc surface roughness. Calculation of etch depths from the ^{51}Cr radioassays assumes that etching is homogeneous in composition. A constant etch rate (by weight) was confirmed in a single experiment by periodically weighing a disc during etching. Etching is indeed homogeneous, as established by following Fe, Cr, Ni and Co (trace) in the etchant. These latter stainless steel constituents were measured by periodic radioassays of the etchant for radioactive ^{51}Cr, ^{59}Fe, ^{58}Co, and ^{60}Co by gamma spectroscopy. Etchant and disc compositions were in close agreement. Microscopic examination of a disc revealed that pitting corrosion occurs, but the pit concentration is too small to affect significantly the etch depth determination. Surface roughness was ignored. Since discs are polished to a 0.05-μm finish and etching smoothes the surface, roughness is expected to distort the etch depth during only the very early etching history.

2.2. Results and discussion

Values of $C(x)$, the tritium concentration, as a function of etch depth x were derived from an etching experiment in two ways. In the first, $C(x)$ is approximated by the volume-average concentration $\overline{C(x)}$ computed as follows for a disc of unit cross-sectional area:

$$C(x) \approx \overline{C(x)} = \frac{N(x_2) - N(x_1)}{x_2 - x_1}, \tag{2}$$

where $N(x_2)$ and $N(x_1)$ are the cumulative amounts of tritium released during etching up to etch depths x_2 and x_1, respectively. This approximation is very good if $x_2 - x_1$ is small, which is true in the work reported here. Moreover, when the latter condition is satisfied, this estimate of $C(x)$ is assigned with confidence to the midpoint of the interval $x_2 - x_1$. In the second method, an unbiased, polynomial, least-squares analysis of the $N(x)$ data is performed. The best fit provided by this analysis is a quadratic in x (correlation coefficient = 0.998). Differentiation of this quadratic with respect to x yields an equation for $C(x)$ linear in x. The following example was obtained from one of four discs injected with tritium:

$$C(x) = 20.0\left[1 - \frac{x}{18.7}\right], \tag{3}$$

where $C(x)$ has units of MBq cm^{-3} and x units of μm.

A plot of Eq. (3) is shown in Fig. 1. When extrapolated to $C(x) = 0$, the straight line gives an x-intercept of 18.7 μm, an estimate of the range of a 2.72-MeV triton in 304–S.S. With the exception of the point labeled 3, and possibly of those labeled 1 and 2, the nine values of $C(x)$ based on the first method are in satisfactory agreement with the least-squares derivative line of the second method. Point 1 is not always observed in replicate discs. Furthermore, the point 1 concentration is small with a large relative radioassay uncertainty, suggesting a suspect relevancy. Points 2 and 3 are always observed, with point 2 lying slightly below and point 3 considerably above the least squares derivative line. This behavior is due to the migration of tritium at room temperature during the two-hour warm-up period preceding the start of etching. Support for this conclusion is provided by the root mean square distance $x_{rms} \approx \sqrt{Dt}$ traveled by a diffusing tritium atom in 2 h. x_{rms} is approximately 1 μm based on an extrapolated value of the tritium diffusion constant D in 304–S.S. [26]. In this view, despite liquid nitrogen disc storage, there is sufficient room-temperature time (2 h) prior to etching for as-deposited tritium to migrate to the surface oxide and become trapped there. As a result, $C(x)$ is enhanced at the surface and depressed just below it. In none of the four discs was there evidence for a weak tail in $C(x)$ be-

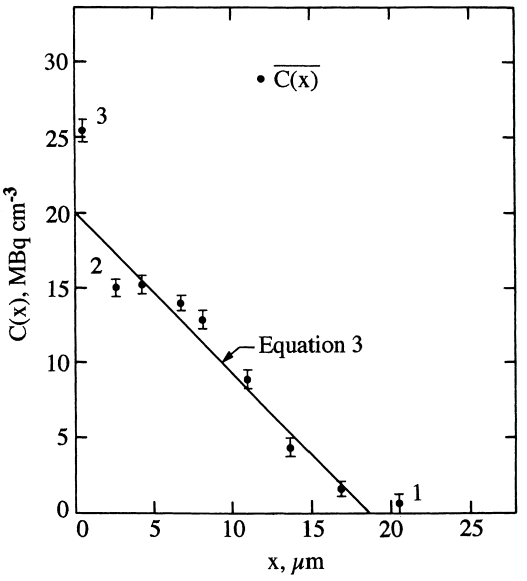

Fig. 1. Tritium concentration versus depth x in 304-S.S. disc ($I = 2\sigma$ uncertainty in ^3H radioassay).

yond the range R_t, as reported by Austin [7]. Insufficient sensitivity of our tritium radioassay method may be responsible.

As the foregoing discussion implies, tritium migration at ambient reactor temperature should distort the initial tritium distribution. Fig. 2 presents $C(x)$ profiles in two discs, one injected at the usual liquid nitrogen temperature (Fig. 1) and the other at ambient reactor temperature. Reactor in-time and power level were identical for both. It is clear that significant tritium migration occurs in an uncooled disc, resulting in a distorted $C(x)$ profile. In a study of the tritium distribution in triton-injected aluminum, others [27] speculated that this same effect was occurring.

The derivative line in Fig. 1 and those from three other replicate discs are plotted in Fig. 3 to demonstrate the reproducibility of the $C(x)$ profiles. For each disc, $C(x)$ has been normalized to its extrapolated value of C_{ex} at $x=0$ to better compare the four profiles. The average of the four triton ranges derived from the profiles is 18.0 ± 1.0 μm, where the uncertainty is the standard deviation. This value agrees favorably with a value of 16.9 μm for a 2.72-MeV triton generated by the SRIM code [22], as well as two predictions based on the Janni tables [28] and the Bragg–Kleeman (BK) rule [29]. Austin [7] reported a value of 20.8 μm in his experimental work.

Further tests of the data utilize Eqs. (4) and (5) to supply values of N_t and R_s for comparison with estimates from other sources. N_t is the cumulative amount of tritium deposited in the target. Eq. (5) is derived in Section 3.

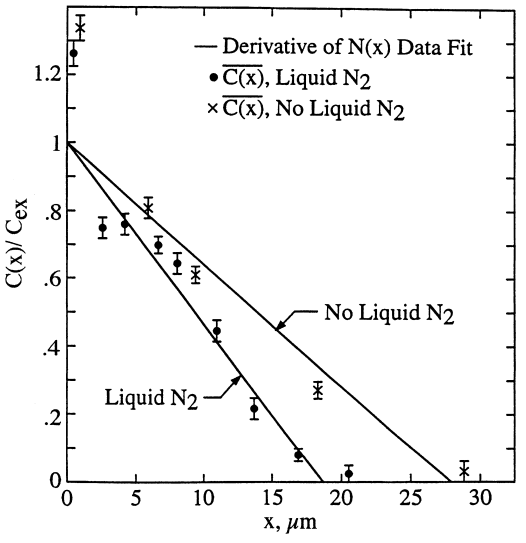

Fig. 2. Effect of disc temperature during recoil injection on the concentration of tritium in 304-S.S ($I=2\sigma$ uncertainty in ^3H radioassay).

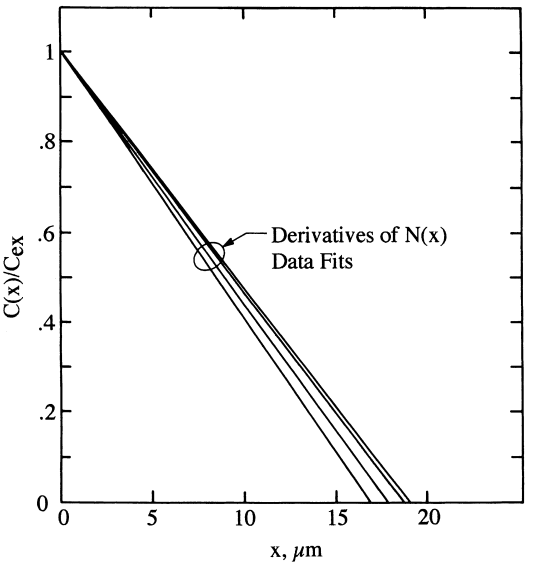

Fig. 3. Tritium concentration (normalized) in four 304-S.S. discs.

$$N_t = \frac{C_{ex} R_t}{2}, \tag{4}$$

$$R_s = \frac{4N_t}{Gt} = \frac{4N_t}{G_w \rho_s t}. \tag{5}$$

For each of the four discs in Fig. 3, the value of N_t in Eq. (4) is in good agreement with N_t from acid etching. This agreement supports (a) the physical interpretation of C_{ex}, i.e. it is the initial tritium concentration at $x=0$, and (b) a cause/effect relationship exists between tritium enhancement observed at the disc surface and the accompanying tritium depression in the disc subsurface. G_w is the triton generation rate (by weight), and ρ_s is the bulk (tap) powder density. The former was measured by dissolving Li_2CO_3 powder from each of the four discs (Fig. 3) in water, followed by tritium (HTO) radioassay. Tritium released as HT during dissolution is negligible. Tritium leakage from the powder prior to dissolution is minimized by storing it at liquid nitrogen temperature. The four discs yield an average R_s of 118 ± 6 μm, where the uncertainty is the standard deviation. For comparison, the SRIM code provides a value of 94.5 μm for a 2.72-MeV triton. Two theoretical estimates of R_s are available by scaling proton ranges in elemental Li, C and O in the Janni tables [28] and applying the heuristic BK and Weighted Reciprocal (WR) rules [29,30] to the Li_2CO_3 powder. This procedure yields values of 88 ± 3.6 and 94 ± 3.8 μm, respectively.

These evaluations show that to a good approximation $C(x_t) = C(x)$ and is linear in x_t for 2.72-MeV tritons.

3. Theory

3.1. DM model

Derivation of the initial recoil concentrations $C(x_t)$ and $C(x_s)$ in a seminfinite source/target slab geometry with arbitrary thicknesses is the objective here. This is best achieved by adopting an approach different from that used by Di Cola and Matzke [1,2]. We consider in Fig. 4, a slab source of monoenergetic recoils: energy E_0, volume generation rate G and generation time t, in contact with a slab target. A recoil of energy E_0 has ranges R_s and R_t in pure source and pure target. A target width of $L_t = R_t$ and a source width of $L_s = 2R_s$ is our example, subsequently called the standard slab. The number of recoils stopping in a target region of width $|x_t|$ (Fig. 4) may be expressed in two different, but equivalent, ways, where the subtended differential solid angle at x_s determines how many are successful. We have

$$\int_{x_t}^{0} C(x_t,t)\,\mathrm{d}x_t = \int_0^{x_{sc}} \int_{\cos\,\theta_1}^{\cos\,\theta_2} -\frac{Gt}{2}\,\mathrm{d}(\cos\,\theta)\,\mathrm{d}x_s + \int_{x_{sc}}^{R_s} \int_{1}^{\cos\,\theta_3} -\frac{Gt}{2}\,\mathrm{d}(\cos\,\theta)\,\mathrm{d}x_s \tag{6}$$

with (Fig. 5) integration limits of

$$\cos\,\theta_2 = \cos\,\theta_3 = \frac{x_s}{R_s}; \quad \cos\,\theta_1 = \frac{x_s}{R_s} - \frac{x_t}{R_t} \tag{7}$$

and

$$x_{sc} = R_s\left[1 - \frac{|x_t|}{R_t}\right] \tag{8}$$

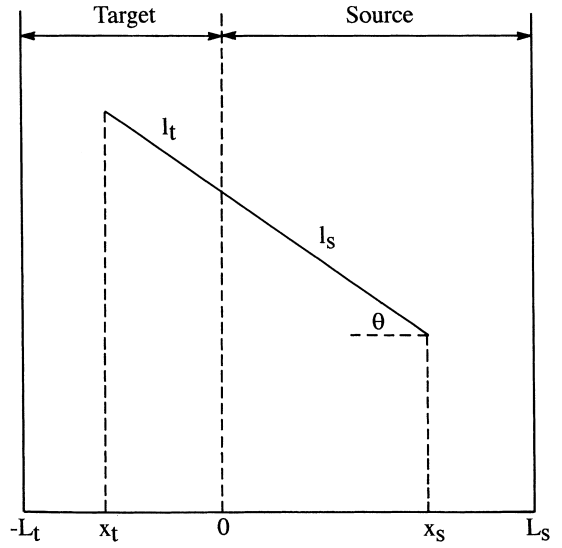

Fig. 4. Trajectory of escaping recoil in slab geometry.

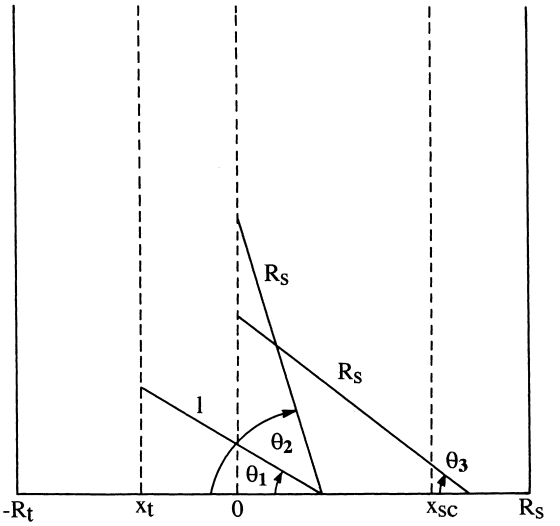

Fig. 5. Limiting trajectories of recoils stopping in target width $|x_t|$ ($L_s \geqslant R_s$).

with l, the total pathlength, defined as follows:

$$l = l_s + l_t. \tag{9}$$

x_{sc} is the straight-ahead ($\theta = 0$) value of l_s in Eq. (1), the linkage equation, resulting in the deposition of a recoil at x_t (Fig. 5). $C(x_t,t)$ is extracted from Eq. (6) by carrying out the integration, followed by differentiation with respect to x_t. The final result is

$$C(x_t,t) = \frac{GtR_s}{2R_t}\left[1 + \frac{x_t}{R_t}\right], \quad -R_t \leqslant x_t \leqslant 0 \tag{10}$$

which agrees with the DM model result for a thick source/target slab.

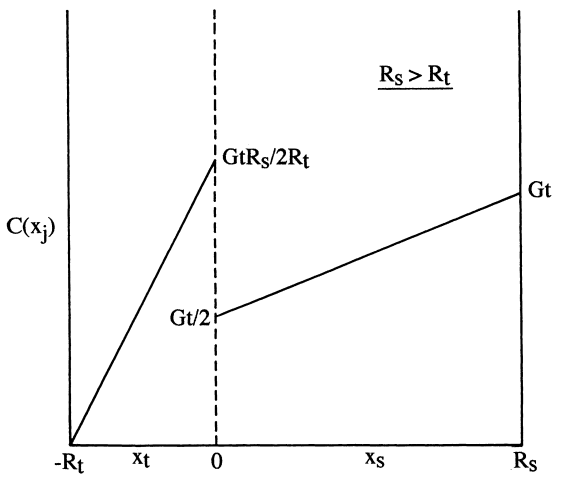

Fig. 6. Initial recoil concentration in standard slab.

$C(x_s,t)$ in the slab source is obtained by using the same solid angle approach, but the linkage equation plays no role:

$$C(x_s,t)=\frac{Gt}{2}\left[1+\frac{x_s}{R_s}\right],\quad 0\leqslant x_s\leqslant R_s. \tag{11}$$

In the interval $R_s\leqslant x_s\leqslant 2R_s$, $C(x_s,t)$ is the mirror image of the concentration profile in Eq. (11), since $x_s=R_s$ is a plane of symmetry in the source. $C(x_t,t)$ and $C(x_s,t)$ are sketched in Fig. 6, where the t dependency there and henceforth is implicit. The recoil concentration is discontinuous at the target/source interface if $R_s/R_t\neq 1$.

The recoil contents of target and source, N_t and N_s, and the two currents $J(0)$ and $J(-L_t)$ round out the recoil description:

$$N_t=\int_{-R_t}^{0}C(x_t)\,dx_t=\frac{GtR_s}{4}, \tag{12}$$

$$N_s=\int_{0}^{R_s}C(x_s)\,dx_s=\frac{3GtR_s}{4}. \tag{13}$$

$J(0)$ and $J(-L_t)$ are the recoil flow rates per unit area at the source/target interface and exterior target boundary. For the standard slab, $J(-L_t)=0$ and

Table 2
Initial recoil concentration in slab geometry

Target	Source
1. $k\leqslant 1$	
1.1. $R_t\geqslant L_t\geqslant \lvert x_{tb}\rvert\geqslant 0$	
$C(x_t)=\frac{GtR_s}{2R_t}\left[1+\frac{x_t}{R_t}\right],-L_t\leqslant x_t\leqslant x_{tb}\leqslant 0$	$C(x_s)=\frac{Gtk}{2},0\leqslant x_s\leqslant kR_s/2$
$C(x_t)=\frac{GtR_sk}{2R_t},x_{tb}\leqslant x_t\leqslant 0$	
$N_t=\frac{GtR_s}{4}\left[1-[1-k]^2-\left[1-\frac{L_t}{R_t}\right]^2\right]$	$N_s=\frac{GtR_sk^2}{2}$
$J(-L_t)=\frac{GR_s}{4}\left[1-\frac{L_t}{R_t}\right]^2$	$J(0)=J(kR_s)=\frac{GR_sk}{4}[2-k]$
1.2. $R_t\geqslant \lvert x_{tb}\rvert\geqslant L_t\geqslant 0$	
$C(x_t)=\frac{GtR_sk}{2R_t},-L_t\leqslant x_t\leqslant 0$	
$N_t=\frac{GtR_sL_tk}{2R_t}$	same as 1.1
$J(-L_t)=\frac{GR_sk}{4}\left[2-k-\frac{2L_t}{R_t}\right]$	
2. $1<k<2$	
$C(x_t)=\frac{GtR_s}{2R_t}\left[1+\frac{x_t}{R_t}\right],-L_t\leqslant x_t\leqslant 0$	$C(x_s)=\frac{Gt}{2}\left[1+\frac{x_s}{R_s}\right],0\leqslant x_s\leqslant x_{sb}$
$N_t=\frac{GtR_s}{4}\left[1-\left[1-\frac{L_t}{R_t}\right]^2\right]$	$C(x_s)=\frac{Gtk}{2},0\leqslant x_{sb}\leqslant x_s\leqslant kR_s/2$
$J(-L_t)=\frac{GR_s}{4}\left[1-\frac{L_t}{R_t}\right]^2$	$N_s=\frac{GtR_s}{2}[2k-1]$
	$J(0)=J(kR_s)=\frac{GR_s}{4}$
3. $k\geqslant 2$	$C(x_s)=\frac{Gt}{2}\left[1+\frac{x_s}{R_s}\right],0\leqslant x_s\leqslant R_s$
same as 2.	$C(x_s)=Gt,R_s\leqslant x_s\leqslant kR_s/2$
	$N_s=\frac{GtR_s}{2}[2k-1]$
	$J(0)=J(kR_s)=\frac{GR_s}{4}$

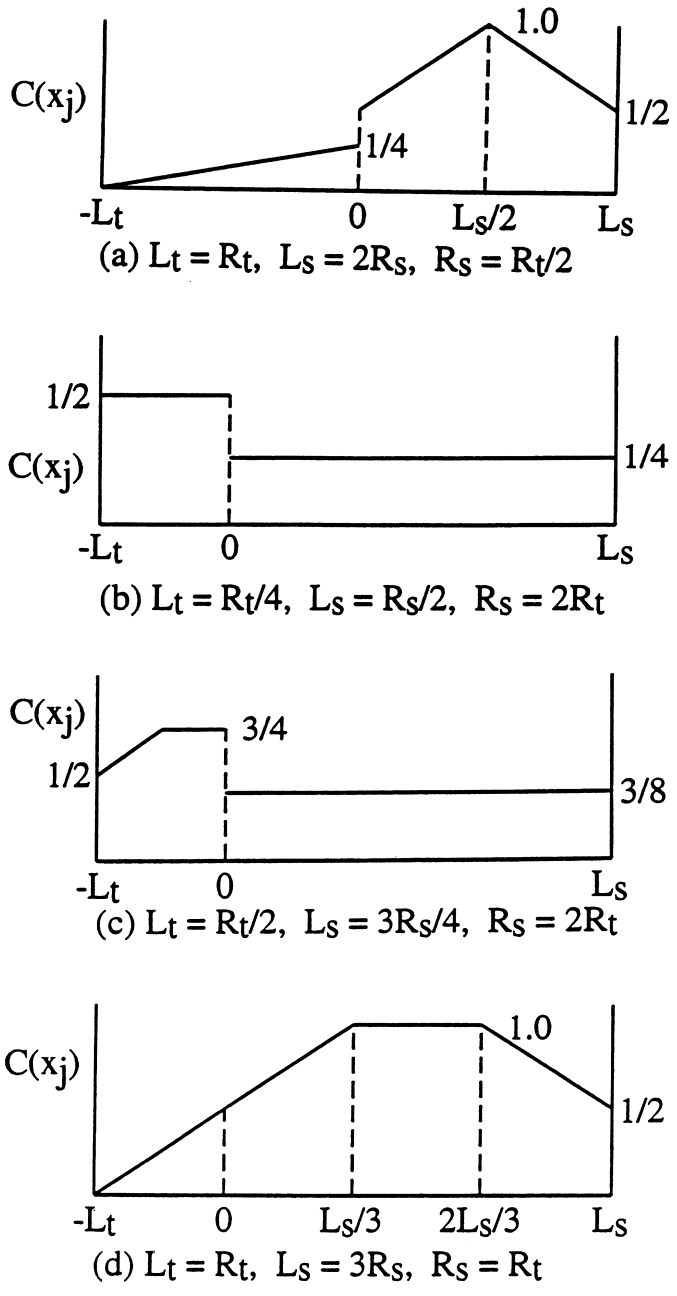

Fig. 7. Initial recoil concentration in slab geometry from Table 2 ($Gt = 1.0$): (a) $L_t = R_t, L_s = 2R_s, R_s = R_t/2$; (b) $L_t = R_t/4$, $L_s = R_s/2, R_s = 2R_t$; (c) $L_t = R_t/2, L_s = 3R_s/4, R_s = 2R_t$; (d) $L_t = R_t, L_s = 3R_s, R_s = R_t$.

$$J(0) = \frac{G}{2}\int_0^{R_s}\int_1^{x_s/R_s} -\mathrm{d}(\cos\,\theta)\,\mathrm{d}x_s = \frac{GR_s}{4} = \frac{N_t}{t}. \qquad (14)$$

The approach used above is readily extended to other target/source thicknesses. In doing so, it is convenient to express L_s in units of R_s, i.e. $L_s = kR_s$. Table 2 lists results for all values of L_s and L_t, and Fig. 7 presents some examples. In this table, the left/right configuration of the target/source and the coordinate system in Fig. 4 are adopted. Breakpoint criteria labeled 1.1 and 1.2 in Table 2 divide the tabular results for $k \leqslant 1$ into two separate fields. The tabular entry for $C(x_s)$ is omitted when $x_s > L_s/2$ because $C(x_s)$ is always symmetrical about the source midplane. In every case, both $C(x_s)$ and $C(x_t)$ are either ramp-like or uniform only, or a combination of the two joined at source and target breakpoints

$x_{sb} = (k-1)R_s$ and $x_{tb} = (k-1)R_t$. A jump discontinuity always occurs at the target/source interface, except when $R_s = R_t$.

DM model predictions above are suspect when significant recoil straggling occurs and/or the linkage equation is no longer a good approximation. Straggling certainly increases as E_0 decreases. A subtle property of the linkage equation is the constraints it places on the energy-dependent target/source recoil stopping powers, pathlengths and ranges. In medium j the range R_j of an as-produced recoil and its pathlengths up to and below energy $E < E_0$ during slowing down ($\rightarrow$) must satisfy the continuity condition

$$l_j(E_0 \rightarrow E) + l_j(E \rightarrow 0) = R_j, \quad E_0 \geqslant E \geqslant 0. \tag{15}$$

Eq. (15) and the linkage equation yield the following constraints:

$$\frac{R_s(E)}{R_t(E)} = \frac{l_s(E_0 \rightarrow E)}{l_t(E_0 \rightarrow E)} = \frac{S_t(E)}{S_s(E)} = \frac{R_s}{R_t}, \tag{16}$$

where $S_j(E)$ and $R_j(E)$ are the stopping power and range of a recoil at energy E. From Eq. (1), we derive

$$l^{-1} = \frac{f_v^s}{R_s} + \frac{f_v^t}{R_t}, \tag{17}$$

where f_v^s and f_v^t are the source and target volume fractions in the slab geometry. Eq. (17) reduces to the WR rule [30], which predicts the range of a charged particle in a homogeneous or heterogeneous mixture. The reduction is complete when l is replaced by its equivalent, the range $R_m(E_0)$ in the mixture (m). Further analysis shows that Eq. (1), the six distinct, binary equalities in Eq. (16), and Eq. (17) are very tightly coupled. For, if any one of these eight is true, the remaining seven are true, proving that the linkage equation is not a unique basis for the derivation of $C(x_t)$ in the DM model.

An interesting side issue concerns the maximization of N_t for a fixed, target/source, overall length of $L = L_s + L_t$. Does a maximum, N_{tm}, exist for every L in the interval $L \leqslant R_s + R_t$? A search for N_{tm} shows that there is a unique pair of L_s and L_t values, L_{sm} and L_{tm}, which maximizes N_t subject to breakpoint criteria $L_t \geqslant |x_{tb}|$ and $L_t \leqslant |x_{tb}|$. These criteria define a special value of L, $L_0 = 2R_sR_t/R_s + R_t$, which divides the scale of L into two regions: $L_0 < L \leqslant R_s + R_t$ and $L \leqslant L_0$. Table 3 summarizes the results of this analysis.

Table 3
Maximization of N_t for fixed $L \leqslant R_s + R_t$

1.	$L_0 < L \leqslant R_s + R_t$
	$L_{sm} = \dfrac{R_s[R_t^2 - R_sR_t + R_sL]}{R_s^2 + R_t^2}$
	L_{tm} = interchange R_s and R_t in L_{sm}
	$N_{tm} = \dfrac{GtR_s}{4}\left[1 - \dfrac{(R_s + R_t - L)^2}{R_s^2 + R_t^2}\right]$
2.	$L \leqslant L_0 \leqslant R_s + R_t$
	$L_{sm} = L_{tm} = \dfrac{L}{2}$
	$N_{tm} = \dfrac{GtL^2}{8R_t}$

3.2. Pathlength and energy distributions

A probabilistic description of the three pathlengths l_s, l_t and l, and the two capture energies, E_e and E_a, adds considerably to an understanding of recoil behavior in the DM model, and provides, too, additional testing opportunities with the SRIM code. E_e, the escape energy, is the recoil energy spent in the target, while $E_a = E_0 - E_e$ is the recoil energy absorbed by the source.

We now derive the probability density functions (pdf) of these five variates. Like $C(x_s)$ and $C(x_t)$, the pdf's depend on the values of R_s, R_t, L_s and L_t. For the standard slab in Fig. 6, we choose to examine only the population of escape recoils; that is, recoils generated in $0 \leqslant x_s \leqslant R_s$ which exit the source and stop in the target. $p(l_s)$ is the seminal p.d.f. $p(l_s)\,\mathrm{d}l_s$ is the unconditional probability that l_s of an escaping recoil lies in $\mathrm{d}l_s$ about l_s. Consider a horizontal slice of the source with unit cross-sectional area. $J(0)$ from this slice of thickness R_s is $GR_s/4$. The differential solid angle alone determines the number of escape pathlengths of length l_s to $l_s + \mathrm{d}l_s$ generated by isotropic recoil emission in $\mathrm{d}x_s$ about x_s. We write

$$p(l_s)\,\mathrm{d}l_s = \frac{\int_0^{l_s} -\frac{Gt}{2}\,\mathrm{d}x_s\mathrm{d}(\cos\,\theta)}{J(0)t} \tag{18}$$

Since $x_s = l_s \cos\,\theta$, Eq. (18) yields after the integration

$$p(l_s) = \frac{1}{R_s}, \quad 0 \leqslant l_s \leqslant R_s. \tag{19}$$

So, with some surprise, we find that source pathlengths of escape recoils are distributed uniformly in the domain $0 \leqslant l_s \leqslant R_s$. $p(l_s)$ is the source of $p(l_t)$ and $p(l)$ by the following transformation:

$$p(v) = p(l_s)\left|\frac{\mathrm{d}l_s}{\mathrm{d}v}\right|, \quad v = l_t, l \tag{20}$$

because a one-to-one correspondence between l_s and v exists in each case. We find that these two pdf's are uniform also:

$$p(l_t) = \frac{1}{R_t}, \quad 0 \leqslant l_t \leqslant R_t, \tag{21}$$

$$p(l) = \frac{1}{R_s - R_t}; \quad R_t \leqslant l \leqslant R_s, \;\; R_s > R_t, \tag{22}$$

$$p(l) = \text{interchange } R_s \text{ and } R_t \text{ in Eq. (22) when } R_s < R_t. \tag{23}$$

An additional feature must be added to the DM model in order to derive $p(E_e)$ and $p(E_a)$, because the

linkage equation alone provides no information on how the energy of the recoil changes along its trajectory. As discussed in the next section of this paper, SRIM results suggest the following relationship:

$$E_e = E_0\left[1 - \frac{l_s}{R_s}\right]^{\gamma}; \quad \gamma = \text{constant}. \tag{24}$$

Eqs. (19), (20) and (24) with $v = E_e, E_a$ yield both pdf's:

$$p(E_e) = \frac{E_e^{1-\gamma/\gamma}}{\gamma E_0^{1/\gamma}}, \quad 0 \leqslant E_e \leqslant E_0, \tag{25}$$

$$p(E_a) = \frac{[E_0 - E_a]^{1-\gamma/\gamma}}{\gamma E_0^{1/\gamma}}, \quad 0 \leqslant E_a \leqslant E_0. \tag{26}$$

$p(E_e)$ and $p(E_a)$ are mirror images, the shapes of which are sensitive to the value of γ. The mean values of E_e and E_a are $E_0/1+\gamma$ and $E_0\gamma/1+\gamma$, respectively.

These five pdf's do not apply when the source/target configuration differs from the standard slab or when some other choice for the recoil population, e.g., generated recoils instead of escaping recoils, is made. Under these circumstances the pdf's are derived using the same mathematical approach.

4. SRIM results

In a Monte Carlo simulation with the SRIM code, a recoil's origin and initial direction in the source are randomly selected. For 2.72-MeV tritons, Fig. 8 presents the $C(x_j)$ profile produced by the SRIM code in Li_2CO_3/304-S.S. $C(x_s)$ predicted by DM theory is in good agreement with the SRIM values, while SRIM values of $C(x_t)$, in contrast with the DM linear profile, trail off as $|x_t|/R_t$ increases. Additional SRIM runs show that DM predictions are less satisfactory as E_0 decreases. The 5-keV results in Fig. 9 provide a good example, although the disagreement in both source and target is already noticeable at $E_0 = 30$ keV. Range straggling and backscattering dominate the $C(x_j)$ profiles for 5-keV tritons. In this case, some 30% of the tritons entering the target are backscattered, producing a ramp-like rise in $C(x_s)$ as the source/target interface is approached. It can be shown that the dip in $C(x_s)$ at the free surface is expected when significant range straggling occurs in the source.

For each triton, the Monte Carlo option in SRIM supplies the coordinates identifying triton birth, death and medium crossover, as well as the crossover energy E_e. The Code outputs yield by separate computations

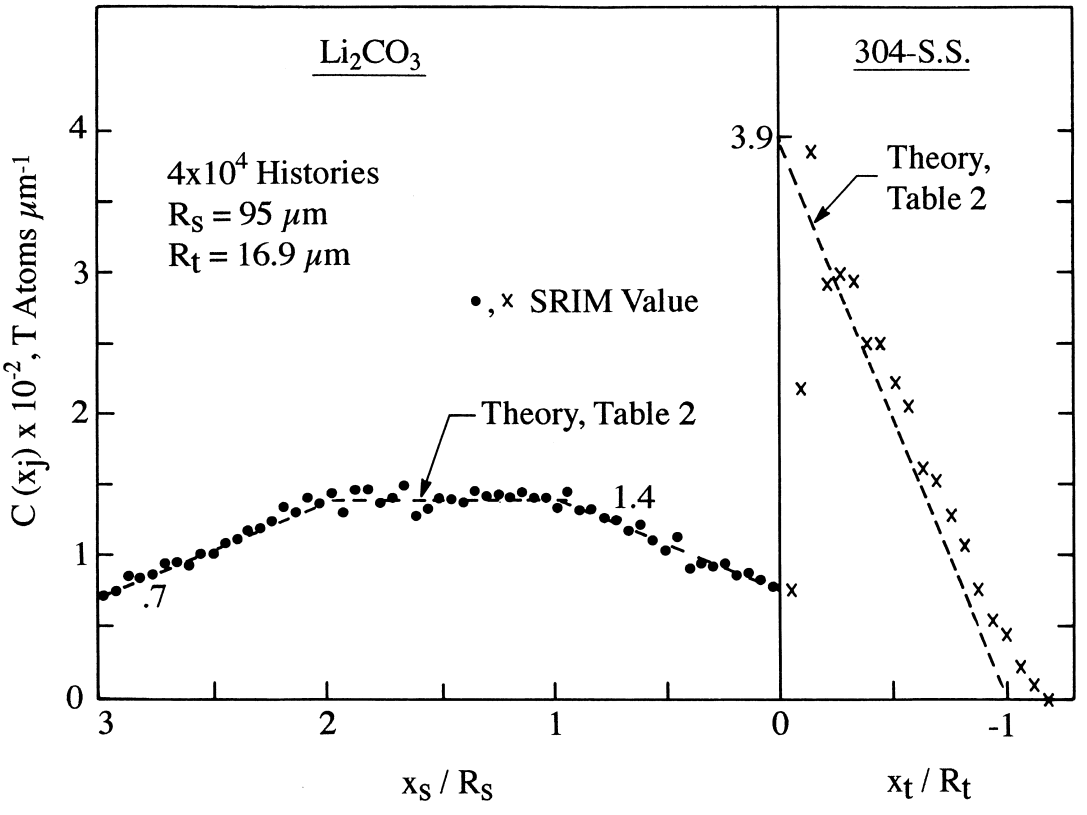

Fig. 8. Initial tritium concentration in Li_2CO_3/304-S.S. slab ($E_0 = 2.72$ MeV, $L_s = 3R_s$, $L_t = 2R_t$).

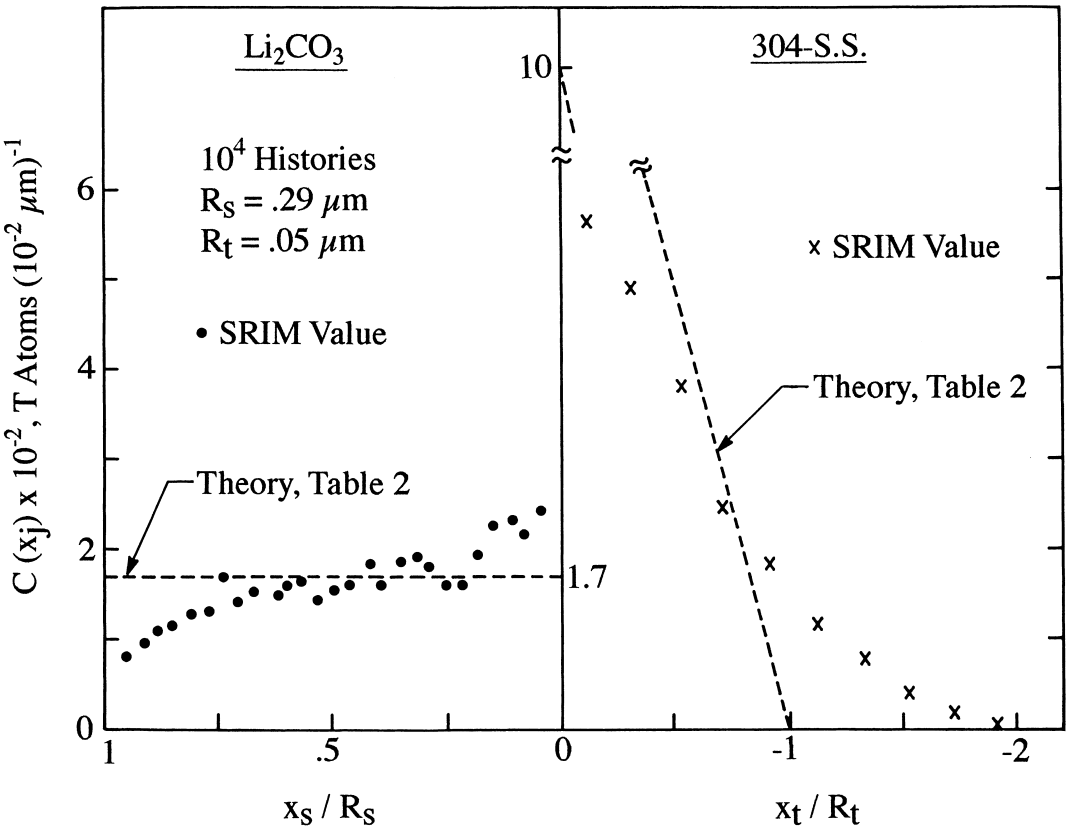

Fig. 9. Initial tritium concentration in Li_2CO_3/304-S.S. slab ($E_0 = 5$ keV, $L_s = R_s$, $L_t = 3R_t$).

l_s, l_t and E_e, and the three corresponding pdf's. Fig. 10 (a) and (b) show for 2.72-MeV tritons that SRIM and DM l_s and l_t pdf's are in satisfactory agreement. An adequate basis for the theoretical $p(E_e)$ is to find the simplest algebraic form that (a) correlates E with the SRIM value of l_j, and (b) satisfies both the necessary condition $S_j > 0$ and the constraints of DM theory in Eq. (16). Eq. (24) is a satisfactory candidate. We note that Eq. (16) mandates identical values of γ in source and target. $p(E_e)$ from a SRIM run is presented in Fig. 10(c), where $p(E_e)$ from Eq. (24) with $\gamma = 3/4$ follows the general trend of the SRIM data points. Fig. 11 shows the pdf's for 5-keV tritons, and, again, the basis for the theoretical $p(E_e)$ is Eq. (24). At this low value of E_0 the l_s and l_t pdf predictions of DM theory are in substantial disagreement with SRIM results. Except for scale, the SRIM values in Fig. 10(c) and 11(c) follow the same trend. Eq. (24) with a single value of γ, however, provides only a marginal fit of E/E_0 vs. l_j/R_j in the source and target. A comparison of SRIM values with theory is therefore moot.

Differentiation of Eq. (24) yields the triton stopping power:

$$S_j \propto 1/E^{\alpha}; \quad j = s, t, \tag{27}$$

where $\alpha = 1 - \gamma/\gamma$. The above S_j or Eq. (24) is a sufficient, but not a necessary, condition validating Eqs. (1), (16) and (17). However, the approximate nature of Eq. (24) is reflected in two, non-physical S_j features. S_j is singular at $E = 0$, and S_j does not pass through a maximum during triton slowing down from $E_0 > 1$ MeV, say.

An important test of DM theory is how well SRIM results validate Eqs. (1) and (16). In general, satisfactory agreement (within 5%) with these DM equations is observed for $E_0 = 2.72$ MeV, except at low values of E. S_t/S_s is a sensitive parameter in such a test, and according to the SRIM tables this ratio falls with decreasing triton energy E. At $E = 50$ and 10 keV, for example, SRIM values of S_t/S_s are 11% and 43% smaller, respectively, than the SRIM value at $E = 2.72$ MeV. In contrast, the DM value of S_t/S_s in Eq. (16) equals $R_s/R_t = 5.5$, a constant.

Finally, exploratory SRIM runs suggest that DM theory may be useful in a wider context. Up to $E_0 = 10$ MeV, say, the utilities of Eqs. (1) and (24) are readily confirmed for O, P, Fe, Xe and Rn recoils in Li_2CO_3/304-S.S.

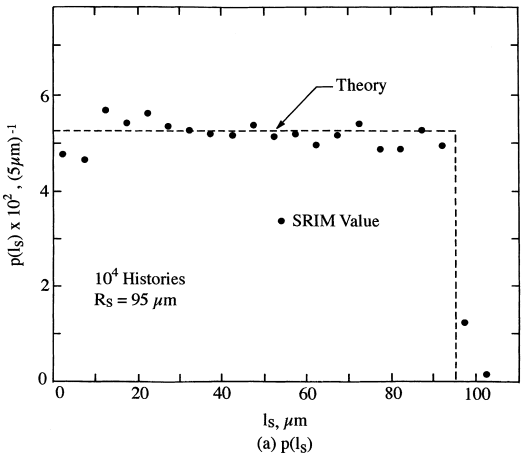

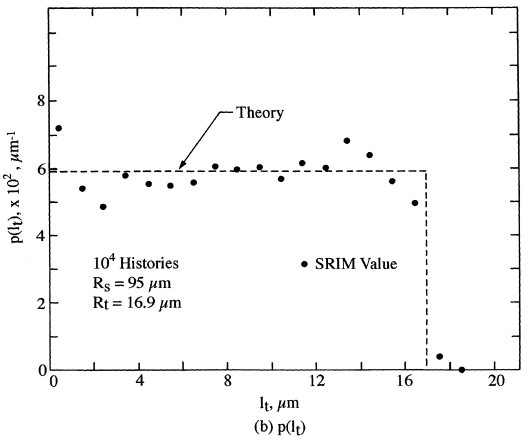

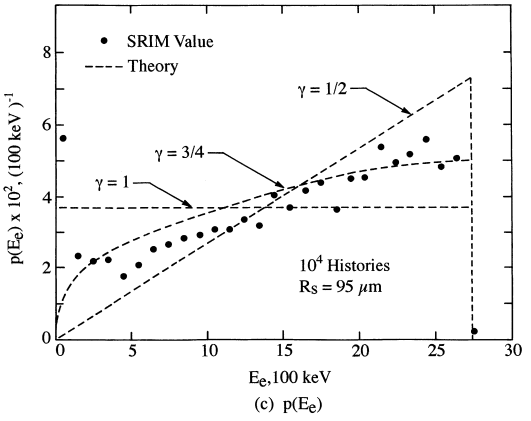

Fig. 10. pdf's for 2.72-MeV tritons in Li_2CO_3/304-S.S. slab ($L_s = R_s$, $L_t = 2R_t$): (a) $p(l_s)$; (b) $p(l_t)$; (c) $p(E_e)$.

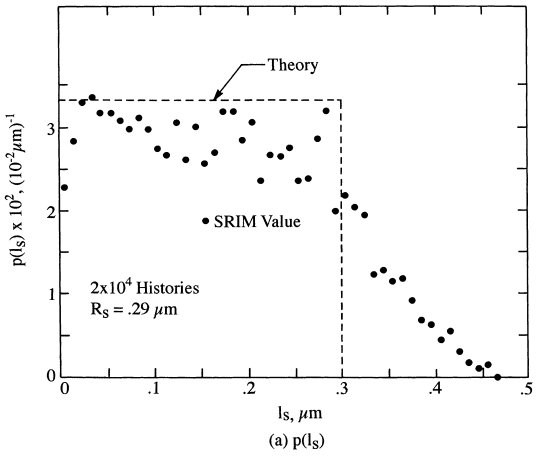

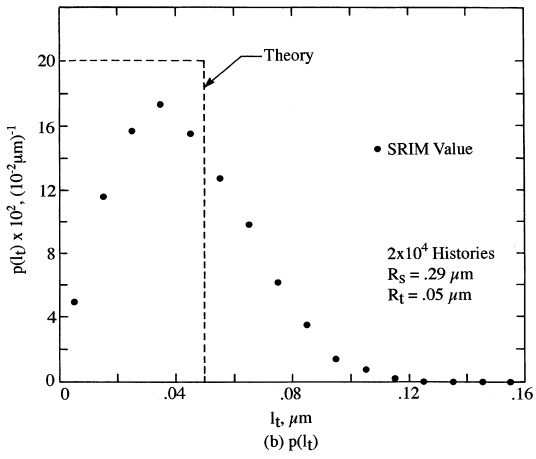

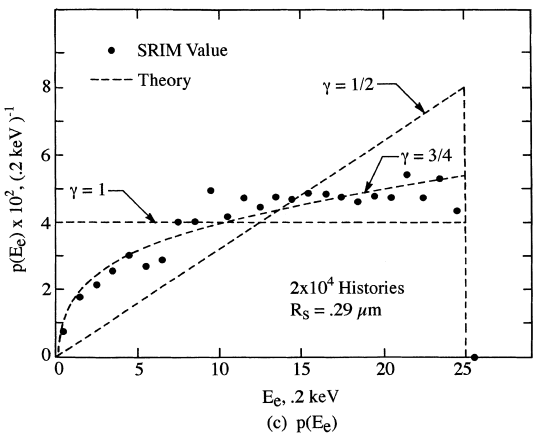

Fig. 11. pdf's for 5-keV tritons in Li_2CO_3/304-S.S. slab ($L_s = R_s$, $L_t = 3R_t$): (a) $p(l_s)$; (b) $p(l_t)$; (c) $p(E_e)$.

5. Conclusions

The experimental concentration profile of 2.72-MeV recoil tritium in a thick 304-S.S. target is in satisfactory agreement with the linear profile predicted by DM theory. Monte Carlo simulations with the SRIM code reveal, however, that the profile is generally non-linear, and increasingly so for tritons with decreasing initial energies below 2.72 MeV. Confirmation of a non-linearity in the

experimental concentration profile was not possible because of insufficient sensitivity of the tritium radioassay.

Acknowledgements

A grant from EG&G Mound Applied Technologies provided one of us (A.R.D.) with partial financial support during his PhD program at The Pennsylvania State University.

References

[1] G. Di Cola, Hj. Matzke, Nucl. Instrum. Meth. 57 (1967) 341.
[2] G. Di Cola, Hj. Matzke, Euratom Report EUR 2157.e (1964).
[3] R.H. Barnes, T.S. Elleman, D.N. Sunderman, in: Second Nuclear Conference on Reactor Chemistry, Gatlingburg, Tennessee, 1961, p. 245.
[4] D.L. Morrison, R.H. Barnes, T.S. Elleman, D.N. Sunderman, Battelle Institute Report BMI-1592 (1962).
[5] D.L. Morrison, T.S. Elleman, D.N. Sunderman, J. Appl. Phys. 35 (1964) 1616.
[6] A. Bauer, J. Bugl, G.G. Cocks, T.S. Elleman, J.E. Howes, D.L. Morrison, F.R. Winslow, Battelle Institute Report BMI-1611 (1963).
[7] J.H. Austin, T.S. Elleman, J. Nucl. Mater. 43 (1972) 119.
[8] J.H. Austin, T.S. Elleman, K. Verghese, J. Nucl. Mater. 48 (1973) 307.
[9] K. Hashizume, M. Sugisaki, K. Hatano, T. Ohmori, J. Nucl. Sci. Technol. 31 (1994) 1294.
[10] A. Yokoyama, M. Nakashima, E. Tachikawa, J. Nucl. Mater. 101 (1981) 9.
[11] R.D. Calder, T.S. Elleman, K. Verghese, J. Nucl. Mater. 46 (1973) 46.
[12] T.S. Elleman, K. Verghese, J. Nucl. Mater. 53 (1974) 299.
[13] C.W. Pennington, T.S. Elleman, K. Verghese, Nucl. Technol. 22 (1974) 405.
[14] A. Ong, T.S. Elleman, Nucl. Instrum. Meth. 86 (1970) 117.
[15] K. Hashizume, Y. Hatano, K. Sakamoto, M. Sugisaki, Fusion Technol. 28 (1995) 1175.
[16] G. Di Cola, Hj. Matzke, Euratom Report EUR 3488.e (1967).
[17] S. Flugge, K.E. Zimen, Z. Phys. Chem. 42 (1939) 179.
[18] W. Inthoff, K.E. Zimen, Trans. Chalmers. Univ. Techn. (Göteborg), 1956, no. 176.
[19] H. Gaus, Z. Naturf. A 16 (1961) 1130.
[20] R. Lindner, Hj. Matzke, Z. Naturf. A 15 (1960) 1082.
[21] G.S. Randhawa, H.S. Virk, Radiat. Measur. 26 (1996) 541.
[22] J.F. Ziegler, SRIM-96, IBM-Research, Yorktown, NY (1995).
[23] A.R. Dulloo, PhD Thesis, The Pennsylvania State University (1996).
[24] A.B. Antoniazzi, W.T. Shmayda, Fusion Technol. 26 (1994) 673.
[25] Y. Belot, H. Camus, S. Raviart, A.B. Antoniazzi, W.T. Shmayda, Fusion Technol. 28 (1995) 1138.
[26] T. Hirabayashi, M. Saeki, J. Nucl. Mater. 120 (1984) 309.
[27] M. Nakashima, Y. Aratono, E. Tachikawa, J. Nucl. Mater. 98 (1981) 27.
[28] J.F. Janni, Atom. Data 27 (1982) 147.
[29] N. Tsoulfanidis, Measurement and Detection of Radiation, Hemisphere, Washington, DC, 1983, p. 126.
[30] G. Friedlander, J.W. Kennedy, E.S. Macias, J.M. Miller, Nuclear and Radiochemistry, Wiley, New York, 1981, p. 218.